

An Australia Telescope survey for CMB anisotropies

Ravi Subrahmanyam,^{1,2} Michael J. Kesteven,¹ Ronald D. Ekers,¹ Malcolm Sinclair¹ and Joseph Silk³

¹Australia Telescope National Facility, CSIRO, PO Box 76, Epping, NSW 2121, Australia

²Raman Research Institute, Sadashivanagar, Bangalore 560 080, India

³Departments of Astronomy and Physics and Centre for Particle Astrophysics, University of California, Berkeley, CA 94720, USA

Accepted 2000 February 8. Received 2000 February 8; in original form 1999 August 18

ABSTRACT

We have surveyed six distinct ‘empty fields’ using the Australia Telescope Compact Array (ATCA) in an ultracompact configuration with the aim of imaging, with a high brightness sensitivity, any arcminute-scale brightness-temperature anisotropies in the background radio sky. The six well-separated regions were observed at a frequency of 8.7 GHz, and the survey regions were limited by the ATCA primary beams which have a full width at half-maximum of 6 arcmin at this frequency; all fields were observed with a resolution of 2 arcmin and an rms thermal noise of $24 \mu\text{Jy beam}^{-1}$. After subtracting foreground confusion detected in higher resolution images of the fields, residual fluctuations in Stokes I images are consistent with the expectations from thermal noise and weaker (unidentified) foreground sources; the Stokes Q and U images are consistent with expectations from thermal noise.

Within the sensitivity of our observations, we have no reason to believe that there are any Sunyaev–Zeldovich holes in the microwave sky surveyed. Assuming Gaussian-form CMB anisotropy with a ‘flat’ spectrum, we derive 95 per cent confidence upper limits of $Q_{\text{flat}} < 10\text{--}11 \mu\text{K}$ in polarized intensity and $Q_{\text{flat}} < 25 \mu\text{K}$ in total intensity. The ATCA filter function peaks at $l = 4700$ and has half-maximum values at $l = 3350$ and 6050.

Key words: techniques: interferometric – cosmic microwave background – cosmology: observations – radio continuum: general.

1 INTRODUCTION

Today, we are fairly confident that the large-scale structure grew out of primordial seed perturbations by gravitational instabilities in a dark matter-dominated universe. The physics that dominates the coupling between matter inhomogeneities and the cosmic microwave background (CMB) radiation anisotropies is different on different angular scales, and the multifarious coupling mechanisms are believed to result in a complicated spectrum of radiation anisotropies (see, e.g., Hu, Sugiyama & Silk 1997 for a recent review).

The primary anisotropies in the CMB that result from subhorizon couplings via gravitational, Doppler and acoustic effects are expected to create features in the anisotropy spectrum on angular scales exceeding several arcmin; the cut-off at small angular scales depends on photon diffusion, recombination physics, any reionization at late epochs, and the cosmological parameters that determine the angular size–redshift relation. Improvements in the precision of measurements of the band powers in anisotropies in the CMB, combined with large-scale-structure observations, lead to refinements in the parameters of the background cosmology, models for structure generation, and the matter content of the universe (see Bond & Jaffe 1998, Gawiser &

Silk 1998 and Lawrence, Scott & White 1999 for examples of the values of CMB anisotropy measurements in constraining structure formation models).

The power in the CMB anisotropy spectrum towards small angular scales is expected to be strongly damped: the spectral cut-off may constrain the ionization history of the primordial gas and mechanisms for reionization (Dodelson & Jubas 1995). Reionization may erase primary anisotropies on small angular scale; however, via the ‘Vishniac effect’, reionization may generate secondary fluctuations of significant magnitude (Hu, Scott & Silk 1994). Gravitational lensing by large-scale structure may also transfer anisotropy power from larger to smaller scales, enhancing the amplitude of primary anisotropies at small scales (Metcalf & Silk 1997). The time dependence of the gravitational potential during late non-linear structure formation may imprint anisotropies on the CMB via the ‘Rees–Sciama effect’, and this may be the dominant anisotropy on subarcminute scales (Seljak 1996). Another plausible source for small-angular-scale anisotropy is the Sunyaev–Zeldovich effect in the relativistic plasma cocoons of radio galaxies (Yamada, Sugiyama & Silk 1999). Anisotropies in the CMB on arcminute scales could also provide a powerful constraint on any cosmological magnetic field (Subramanian & Barrow 1998).

If structure forms by the growth of initial small perturbations, the CMB anisotropies are expected to be partially polarized. This is because the matter inhomogeneities cause the radiation to be anisotropic, and Thomson scattering of the anisotropic radiation at the last-scattering surface generates linear polarization (Bond & Efstathiou 1984; Hu & White 1997). The fractional polarization in the primary anisotropies is expected to be greater at smaller angular scales, and the detection of polarization in the CMB anisotropies may be a fundamental test of, and provide an additional observational constraint on, theories for structure formation.

The secondary anisotropies result from interactions in the post-recombination era and during non-linear structure formation. An important effect here is the Sunyaev–Zeldovich (S–Z) scattering of the CMB as it encounters hot gas in the deep potential wells of clusters of galaxies (see Birkinshaw 1998 for a recent review). The expectations for the CMB anisotropy arising from this effect are difficult to compute, and depend on the abundances of dark matter haloes with cluster masses that are formed at different cosmic epochs, and the processes by which the gas accumulates in these potential wells and is heated. Nevertheless, using models for the evolution of the intracluster medium and estimates of the abundances of cluster potentials from the Press–Schechter formalism or self-similar evolutionary models, distribution functions have been derived for the S–Z sources, and these have been used to estimate the CMB anisotropies in different cosmological models and scenarios for the evolution of the gas (Bartlett & Silk 1994; Markevitch et al. 1994). Blind surveys for S–Z clusters are expected to provide valuable inputs to our understanding of the late stages of structure formation.

A deep radio survey with the VLA in an *HST* medium deep survey field does appear to have detected a radio decrement (Richards et al. 1997); independently, a Ryle Telescope (RT) observation towards a pair of quasars has also shown a ‘hole’ in the radio sky (Jones et al. 1997). In both cases, follow-up observations in the optical and X-ray bands have not revealed any cluster in these directions. Because the Compton y parameter which determines the magnitude of any S–Z decrement towards a hot-gas cluster is distance-independent, the S–Z flux density (the integrated decrement) may be observable to higher redshifts as compared to the optical/X-ray luminosities. The absence of luminous counterparts in other bands indicates that any clusters that may be responsible for the decrements via the S–Z effect should be at moderately high redshifts: the existence of collapsed massive structures at early epochs defies conventional wisdom (Bartlett, Blanchard & Barbosa 1998) and has led to alternative hypotheses for microwave decrements (Natarajan & Sigurdsson 1999).

In 1990 we commenced a programme to search for arcminute-scale anisotropies with the Australia Telescope Compact Array (referred to as the ATCA experiment). The first results based on a deep survey of a single field were reported in Subrahmanyan et al. (1993); the sensitivity was improved with further observations using improved receivers, and the derived upper limits were reported in Subrahmanyan et al. (1998). We have now used the Australia Telescope to improve the sky area covered, and have imaged six independent sky regions with high brightness temperature sensitivity. Our goal was to make a blind search for any ‘holes’ in the microwave sky apart from deriving estimates of the arcminute-scale CMB anisotropy in total intensity and polarization. In this paper we present these observations.

2 ATCA OBSERVATIONS

The Australia Telescope Compact Array (ATCA; see The Australia Telescope 1992) is an E–W array with five 22-m-diameter antennae movable on a railtrack. The best surface brightness sensitivity is achieved when the array is in a close-packed configuration, and we have configured the ATCA in a 122-m array, with the five antennae equispaced along the E–W track on stations 30.6 m apart, for these observations. In this configuration, observations at declinations lower than -50° would be shadowed in some hour angles, and shadowing results in spurious correlations in the baseline pairs involving antennae whose projected areas overlap. The brightness sensitivity in the observations would progressively decrease for fields at higher declinations because of the increase in projected baselines at large hour angles. The 22-m antennae cannot be placed on stations closer than 30.6 m; therefore we have made all observations in fields located about -50° in declination so that the projected spacings between adjacent antennae would be close to the shadowing limit of 22 m over a large range of hour angles. The observations would have the best brightness sensitivity without shadowing related problems.

Most physical mechanisms for primary anisotropies in the CMB result in wavelength-independent fluctuations in the CMB thermodynamic temperature. At centimetre wavelengths, where the sky brightness of the 2.73-K CMB radiation may be approximated by the Rayleigh–Jeans law, these CMB brightness temperature fluctuations may be considered to be wavelength-independent. On small angular scales the dominant cause of CMB temperature anisotropy may be the S–Z effect: this has a wavelength dependence. However, for this effect, a fairly constant temperature decrement is expected at centimetre wavelengths.

The anisotropy power in the CMB sky is usually described in terms of C_l s in multipole l -space, where $C_l = \langle |C_{lm}|^2 \rangle$ and C_{lm} s are the coefficients in the spherical harmonic expansion of the fractional temperature anisotropy on the celestial sphere. The anisotropy variance, which is expected in any differential measurement of the sky brightness temperature, and is made with an l -space window function of octave width, will be about $l(l+1)C_l$; therefore the CMB anisotropy spectrum is usually a plot of $l(l+1)C_l$ versus l . As discussed earlier, the anisotropy power due to primary anisotropies is expected to cut off at small angles and consequently on arcminute scales, the expected variance in most experimental efforts may be expected to be lower if the effective beam is smaller. There have been estimates of the CMB anisotropy spectrum arising from the decrements due to the thermal S–Z effect in a cosmological distribution of clusters containing hot gas; the resulting $l(l+1)C_l$ is fairly flat in the l -space regime corresponding to arcminute scales (Molnar 1998).

In any image made with the ATCA in its ultra compact array configuration with the five 22-m antennae located 30.6 m apart along the E–W track, provided the observations are made at the same times and using receivers with the same system temperatures, the brightness sensitivity (i.e., the rms noise in the image in units of brightness temperature) would be independent of observing frequency. Observations made at higher frequencies would have smaller beams, and the window function corresponding to the measurements would be located higher up in l -space. Consequently, ATCA observations made at higher frequencies would be attempting to make measurements of the CMB spectrum at larger l , but would be less likely to detect any primary

anisotropies. On the other hand, ATCA observations at all frequencies would be equally sensitive to ‘flat-band’ anisotropies.

The ATCA currently operates in the 20-, 13-, 6- and 3-cm wavelength bands; in its ultracompact configuration, the images at all these wavelengths would be confusion-limited at levels above those required to detect most CMB anisotropies. The confusion at these wavelengths arises from unresolved extragalactic synchrotron sources, which typically have a steep flux-density spectrum with a mean spectral index $\alpha \approx -0.6$ (we define the spectral index by the relation $S_\nu \sim \nu^\alpha$). These sources have an integral number count that approximately follows the relation $N(> S) \sim \nu^{-0.6} S^{-1.2} \Omega$, where S is the flux density, ν is the observing frequency, and Ω is the beam solid angle. We may assume that the discrete sources are Poisson random distributed on the sky, and that the rms confusion noise is roughly the flux density at which we may expect one source in every synthesized beam. Because the synthesized beam scales as $\Omega \sim \nu^{-2}$, we may expect the rms confusion noise to scale as $\Delta S \sim \nu^{-2.2}$. The brightness temperature scales as $T \sim S/(\Omega \nu^2)$, and it follows that the rms brightness temperature ‘noise’ on the image would scale as $\Delta T \sim \nu^{-2.2}$. Every octave increase in frequency reduces the confusion noise by a factor of about 4.6; we have therefore opted to make the ATCA CMB anisotropy observations in the highest available 3-cm band.

When observing with the ATCA in the ultracompact 122-m array configuration, with five antennae equispaced 30.6 m apart along the E–W railtrack, images made using just the four 30.6-m baselines – instead of using all 10 baselines – give the highest surface brightness sensitivity. Images made using just the four 30.6-m baselines between adjacent antennae would have an rms thermal noise that is a factor of $\sqrt{10/4}$ larger, and a synthetic beam that is at least 4 times larger in solid angle. Because the brightness temperature sensitivity depends on the rms thermal noise (in units of flux density per beam) and inversely on the beam solid angle, the images made omitting baselines exceeding 30.6 m would have a brightness sensitivity that is at least a factor of $4/\sqrt{10/4}$ better. For this reason, the images that represent the CMB anisotropy search have been constructed using the four 30.6-m baselines alone; images made using the remaining six baselines exceeding 30.6 m have been used to derive the foreground discrete source confusion in the fields.

As discussed in Section 6.1 below, the CMB anisotropy search using the four 30.6-m baselines is sensitive to anisotropy power in an l -space window defined by the telescope filter function. The observations are sensitive to CMB anisotropy with spatial frequencies that are covered by the 30.6-m baseline, and therefore the filter function would have a smaller fractional bandwidth (and appear to be narrower) in the case of observations closer to the celestial pole, where the projected baseline is, on average, larger. As stated above, the observations are restricted to declinations south of -50° to avoid shadowing. Consequently, the brightness sensitivity of the 30.6-m interferometer, as also the fractional

bandwidth covered by the interferometer in l -space, is a maximum for observations at declination -50° . For observations at declination -50° , the 30.6-m baseline would have a projected baseline close to the dish diameter of 22 m for a significant fraction of the observing time; consequently, the filter function would not be narrow.

The half-power width of the synthesized beam for these low-resolution images is about 2 arcmin for 3-cm observations at -50° declination. This beamsize is more or less right for the detection of S–Z anisotropies due to clusters at moderate redshifts.

2.1 Field selection criteria

Four regions were initially selected at about -50° declination, where highest-surface-brightness observations were possible in the 122-m array without shadowing. These were located well off the Galactic plane. The Molonglo 408-MHz survey (Large et al. 1981) lists sources with flux densities exceeding 0.7 Jy at this declination, and is believed to be complete to 1 Jy; the PMN survey at 4.85 GHz (Wright et al. 1994) lists sources exceeding 40 mJy with 90 per cent completeness: the selected regions had no listed sources in either of these catalogues within 30 arcmin of their centres. There are also no strong sources listed in either of these catalogues that are in the vicinity of the selected regions. We have examined the DSS data of the UK Schmidt 2MASS plates of these regions to verify that there are no obvious peculiarities in the optical – no obvious nebulosities, clusters, or higher-than-usual star counts. The coordinates of the centres of the selected regions are in Table 1. Two pairs of regions were selected that were about 12 hr apart in right ascension, so that the deep surveys for CMB anisotropies could be made in 12-hr LST ranges that did not overlap, and the observations could use the entire time the ATCA was specially configured in the 122-m array for the CMB anisotropy experiment.

These four regions were first observed at 20 cm with the ATCA in its 750-m array configuration. The aim was to detect weaker confusing sources in the regions for the purpose of using the images to select a set of small fields for deep 3-cm imaging for CMB anisotropy. The observations were made during 1996 November 14–17, in the 0.75A configuration and using two 64-MHz wide bands centred at 1344 and 1434 MHz. Visibility measurements over spatial wavelengths 360–3400 λ may be expected to be sensitive to confusing sources with angular scales up to a few arcminutes, and these images would be useful in selecting the fields for CMB anisotropy searches on arcminute scales. The absolute flux density scale was set by short observations of PKS 1934–638, whose flux density was adopted to be 15.01 and 14.83 Jy respectively at 1344 and 1434 MHz. Each region was observed for about 11 hr using dual linear polarizations; the arcminute-resolution images had an rms noise of about

Table 1. Regions surveyed for confusion-free fields.

Region	RA(J2000)	Dec.(J2000)	Peak flux density at 20 cm	Total flux density at 20 cm
A	03 28 26.40	$-51^{\circ} 00' 00.00$	16.6 mJy beam $^{-1}$	145 mJy
B	01 43 26.40	$-50^{\circ} 48' 21.60$	19.5 mJy beam $^{-1}$	205 mJy
C	14 39 33.84	$-50^{\circ} 10' 51.42$	16.6 mJy beam $^{-1}$	199 mJy
D	11 45 23.04	$-50^{\circ} 57' 08.64$	21.1 mJy beam $^{-1}$	207 mJy

The peak and total flux densities at 20 cm are quoted for images not corrected for the attenuation due to the primary beam.

Table 2. Fields observed for CMB anisotropies.

Field	RA(J2000)	Dec.(J2000)	Observing time
A2	03 27 07.68	-50 56 22.0	44 hr
B1	01 43 50.84	-50 57 55.0	36 hr
B2	01 42 04.21	-51 00 47.0	47 hr
C1	14 39 36.72	-50 15 15.0	45 hr
D1	11 46 07.71	-51 00 55.0	46 hr
D2	11 44 38.95	-50 55 37.0	46 hr

0.17 mJy beam⁻¹ before any correction was made for the attenuation due to the primary beam.

Sources may be reliably detected in the images with flux density exceeding about 0.5 mJy beam⁻¹. The ATCA primary beam has half-power width of about 33 arcmin at 21 cm. Adopting an integral source count

$$N(> S) = 1966 S_{\text{Jy}}^{-0.76} \text{ sr}^{-1} \quad (1)$$

at 1.4 GHz, based on the differential source counts in the flux density range 1–50 mJy compiled in Windhorst et al. (1985), regions with 33-arcmin diameter may be expected to have about two sources exceeding 25 mJy. The peak and total flux densities in the 20-cm images of the individual regions are also listed in Table 1. No surveyed region has sources exceeding 25 mJy, implying that the four regions surveyed have relatively moderate numbers of the stronger sources.

The imaging for CMB anisotropies was done in the 3-cm wavelength band, where the ATCA primary beam drops to 10 per cent of its peak value at a radial distance of 5 arcmin. In any region with radius 5 arcmin, about three sources may be expected on the average at 21-cm wavelength with flux density exceeding 0.5 mJy. We identified field centres within the four regions surveyed that do not have sources with 21-cm flux densities exceeding about 0.5 mJy within 5-arcmin radii. Assuming a mean spectral index $\alpha = -0.5$, the fields may not be expected to have sources exceeding about 0.2 mJy at 8.7 GHz. A short ATCA observation at 8.7 GHz revealed a >0.5 mJy source in a potential subfield in region A – an inverted spectrum source – and this field centre was consequently rejected.

A total of six field centres were selected for the deep survey at 8.7 GHz; their coordinate centres are listed in Table 2.

2.2 Observing strategy

The strategy adopted was the same as that in previous ATCA searches for CMB anisotropy (Subrahmanyan et al. 1993, 1998). The observations were made during 1997 July 10–29, in the 122B configuration of the ATCA. The five ATCA antennae provided four 31-m baselines, three 61-m baselines, two 92-m baselines and one 122-m baseline. All fields were observed in full Earth-rotation Fourier-synthesis mode using the E–W array in 12-hr sessions so as to obtain visibilities along complete elliptical (u, v)-tracks in the spatial frequency domain. Observations were made in a pair of 128-MHz wide bands centred at 8640 and 8768 MHz. All four polarization products – XX, YY, XY and YX – were measured for every antenna pair between the X and Y orthogonal linearly polarized signals from each antenna. The visibility data were recorded in spectral line mode, with 32 channels covering the 128-MHz bands.

The flux density scale was set by short observations of PKS 1934–638 made daily; the flux density of this primary calibrator

was adopted to be 2.84 and 2.79 Jy respectively at 8640 and 8768 MHz. Secondary calibrator sources were observed in short 3-min scans every 20 min during the observations. The secondary calibrators and the fields were both observed with the antennae pointing at the calibrator sources/field centres, but with the array phased towards a sky position offset 2 min in right ascension and 30 arcmin in declination. This offset between the pointing and phasing centres is not expected to cause any significant visibility amplitude decorrelation within the spectral channels; on the other hand, systematic errors of various kinds that often appear at the phase centre in Fourier-synthesis images would, in our case, be about 36 arcmin from the field centre (pointing centre) and several primary beamwidths away. The visibility data were time-averaged 30 s online.

2.3 Imaging

The visibility data were imaged using the MIRIAD data reduction software.

Because the ATCA correlator has an inherent triangular weighting for the lag-spectrum in the 128-MHz bandwidth mode, alternate channels are redundant in the 33-channel frequency spectrum. Any offsets in the signal sampler levels, or coupling of the sampler clock birdies into the RF signal, are expected to lead to errors in the end channels of the spectrum, and these may spill-over to the even-numbered channels. For these reasons, we rejected all even-numbered channels and the end channels. We also rejected channels numbered 3 and 31 because the signal-to-noise ratio was poor in these channels close to the band edges. A total of 13 useful spectral channels were retained, giving an effective bandwidth of 104 MHz.

The phase centres were changed off-line to coincide with the antenna pointing centres (field centres) by appropriate corrections to the channel visibility phase for the secondary calibrator and field data. The complex antenna gains, the complex spectral response (bandpass) and the polarization leakages were derived from the secondary calibrator observations, and these were used to calibrate the field visibilities. The field visibilities were then averaged over the 13 frequency channels and transformed into the four Stokes parameters.

Images were made from concatenated data bases separately for each of the six fields. No tapering was applied to the visibility data, and the 30-s visibilities were weighted based on the recorded system temperatures to minimize the image noise. Hereinafter, we refer to images made using the 30.6-m baseline visibilities (with spatial wavelengths less than $1 \text{ k}\lambda$) and rejecting all spacings other than those between adjacently located antennae as LR images. Those images made using exclusively the longer spacings exceeding $1 \text{ k}\lambda$ are referred to as HR images. All images were synthesized with 10-arcsec pixels and 512 pixels a side; the choice ensured that the synthesized beams were well oversampled, and the total area imaged well exceeded the primary beamsize. While synthesizing each LR and HR image, the corresponding synthetic beam pattern images were also made, and these point spread function images are referred to as LR-PSF and HR-PSF images. The images were not deconvolved.

In Table 2 are listed the total observing time on each of the six fields; the harmonic mean time per field was 43.6 hr. The average system temperature of the 3-cm ATCA system at the observing frequency was about 42 K (Gough 1994). Given that the observations were made in dual polarization and in a pair of bands each with an effective bandwidth of 104 MHz, and adopting

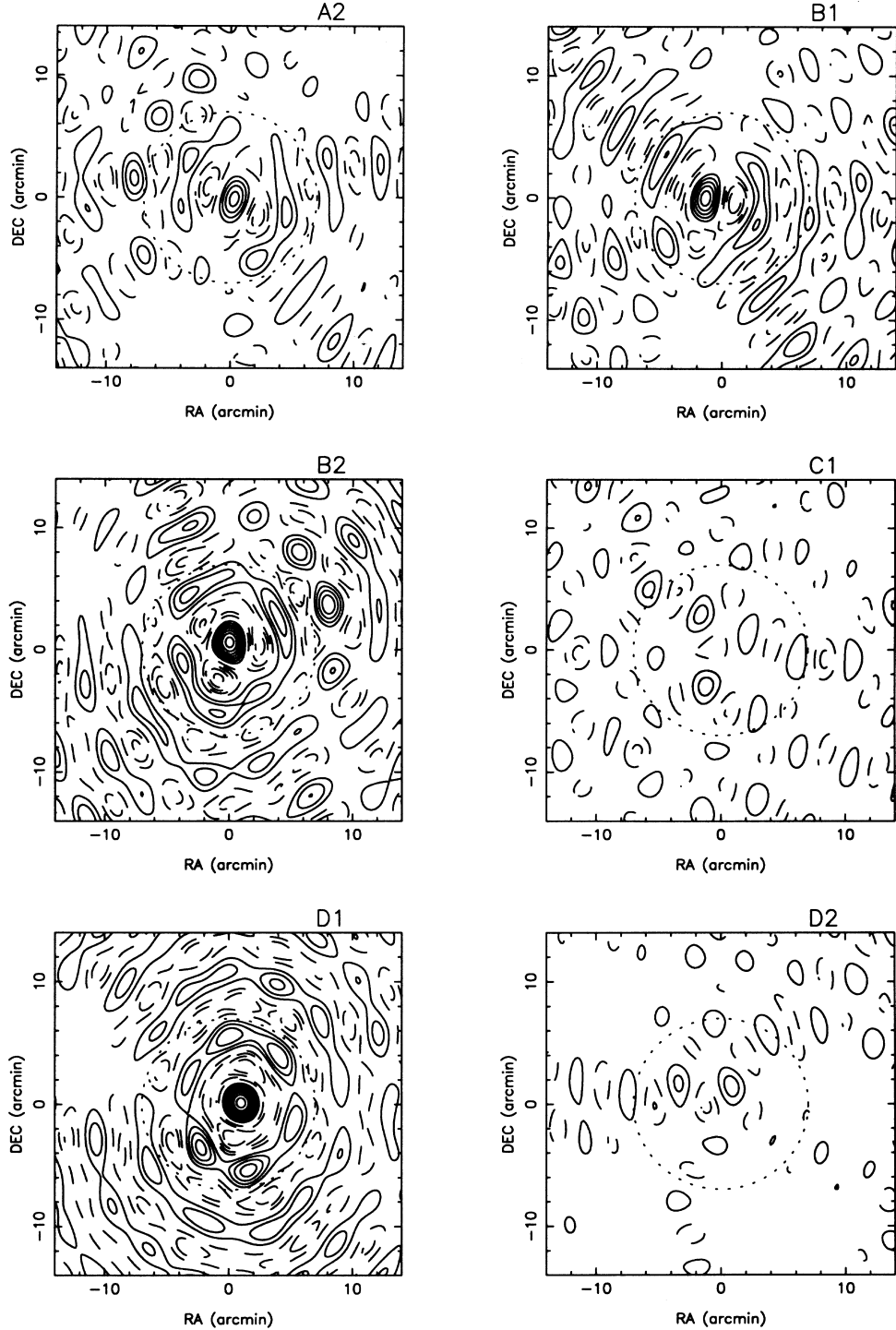


Figure 1. LR images of the six fields in Stokes I made using visibilities in the $0-1\text{k}\lambda$ range. Contours at $24.2\text{ }\mu\text{Jy beam}^{-1} \times (-10, -8, -6, -4, -2, 2, 4, 6, 8, 10, 12, 14, 16)$. In this figure, as also in all the following figures, the locus of the first null in the primary beam pattern is shown as a dotted circle with a 7-arcmin radius.

values of 0.88 for the correlator efficiency and 0.64 for the aperture efficiency of the ATCA antennae, it follows that the ‘naturally weighted’ images made using all the 10 baselines would be expected to have an rms noise of about $15.1\text{ }\mu\text{Jy beam}^{-1}$. The LR images would be expected to have an rms noise that is a factor of $\sqrt{10}/4$ larger, i.e., $23.9\text{ }\mu\text{Jy beam}^{-1}$, and the HR images would be expected to have an rms noise that is a factor of $\sqrt{10}/6$ larger, i.e., $19.5\text{ }\mu\text{Jy beam}^{-1}$.

LR images of the six fields, made in Stokes I , are displayed in Fig. 1 as contour images. HR images of these fields made in Stokes I are displayed in Fig. 2. The images have not been corrected for the attenuation due to the primary beam and have not been deconvolved. The primary beam regions are indicated in the images as dotted circles representing the location of the first null of the primary beams, these have radii of 7 arcmin. We have derived the weighted rms intensity in these images by weighting

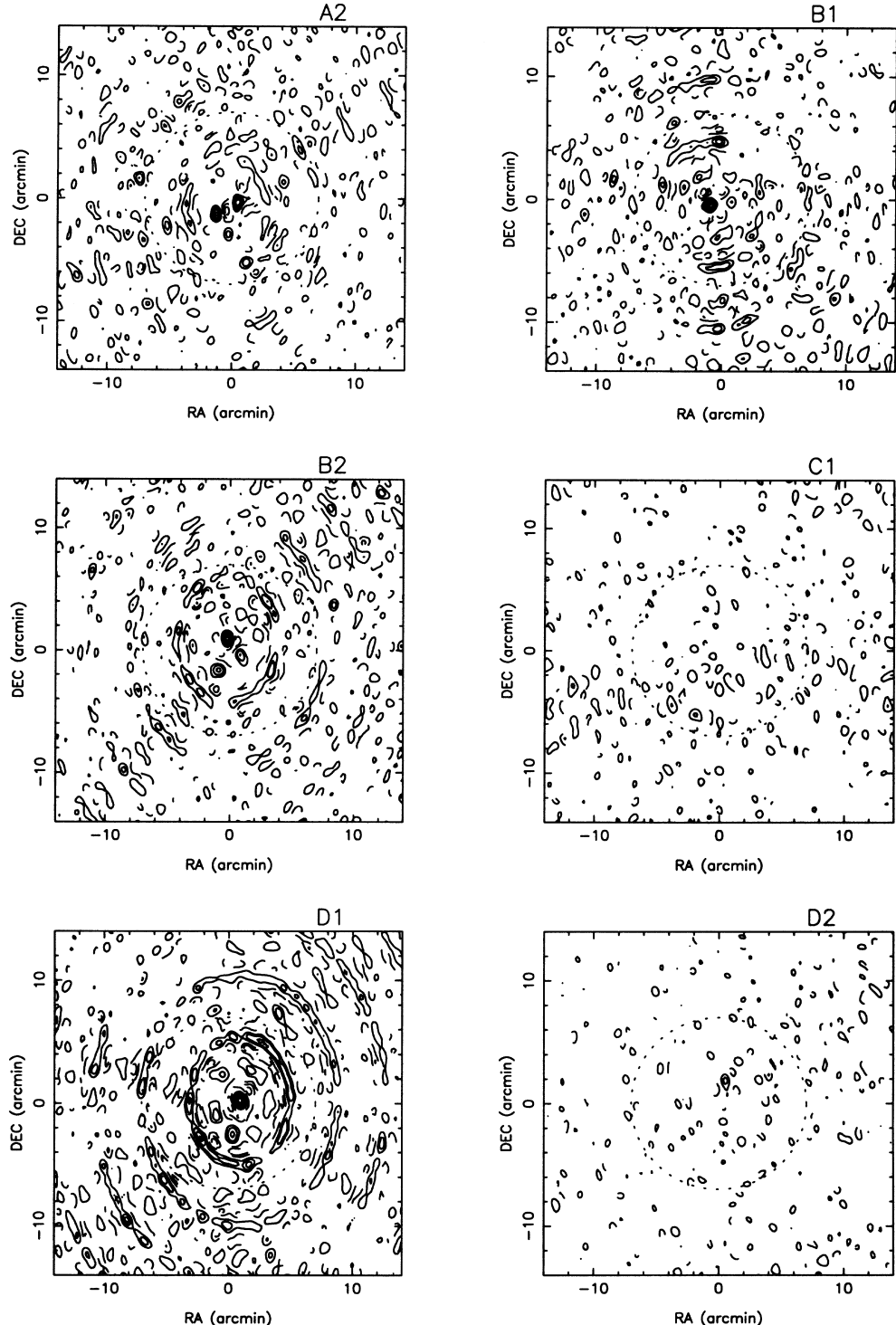


Figure 2. HR images of the six fields in Stokes I made using visibilities exceeding $1\text{k}\lambda$. Contours at $19.5\text{ }\mu\text{Jy beam}^{-1} \times (-6, -4, -2, 2, 4, 6, 8, 10, 12, 14, 16, 18, 20)$.

the image pixel intensities by the value of the primary beam at the pixel locations. These image rms computed for the individual LR and HR images are listed in Table 3.

Most radio sources in the sky have extremely small, if any, circular polarization. Therefore, Stokes V images are expected to be almost entirely thermal noise images. This noise is uniform over synthesized images and does not follow any taper due to the primary beam. We have constructed Stokes V

LR and HR images of the six fields and computed the image rms noise over large areas of the individual images. The rms noise values are listed in Table 3. These represent our best estimates of the thermal noise component of the pixel variances in the images in Figs 1 and 2. It may be noted that the mean variance in these Stokes V images is $(24.2\text{ }\mu\text{Jy beam}^{-1})^2$ for the LR images and $(19.5\text{ }\mu\text{Jy beam}^{-1})^2$ for the HR images. These are within 3 per cent of our

Table 3. Rms pixel intensities in the observed fields.

Field	LR image Stokes <i>I</i>	LR image Stokes <i>V</i>	Residual LR image Stokes <i>I</i>	HR image Stokes <i>I</i>	HR image Stokes <i>V</i>	Residual HR image Stokes <i>I</i>
A2	97.4	23.9	52.3	47.9	19.1	27.8
B1	121.8	26.9	87.9	49.6	21.3	28.5
B2	152.9	23.0	41.1	56.5	18.3	20.9
C1	48.3	25.5	48.3	25.2	20.4	25.2
D1	165.0	23.0	46.0	80.3	19.1	27.3
D2	54.7	22.8	30.3	24.3	18.5	20.1

All rms noise values are in $\mu\text{Jy beam}^{-1}$. The rms in Stokes *I* images were computed from primary-beam weighted intensities.

estimates made above of the thermal noise based on our knowledge of the telescope parameters.

3 FOREGROUND CONFUSION

Clearly, the image rms in Stokes *I* exceeds that expected from thermal noise (the Stokes *V* image rms values); at least in the case of the fields A2, B1, B2 and D1, some part of the excess variance will be due to the discrete sources seen in the corresponding HR images.

3.1 Subtracting confusion models

We have developed an algorithm for modelling the discrete sources in the fields based on the HR images and used these to subtract a significant part of the confusion. The inputs to the algorithm are the LR and HR images of any field, as well as the corresponding synthetic beams: the LR-PSF and HR-PSF images.

The algorithm iteratively identifies point-source components in residual HR images. Whenever point sources are to be subtracted from any image, the corresponding synthesized beam (PSF) image, scaled in amplitude to have a peak equal to the point-source flux density and shifted in sky position to the location of the component, is subtracted.

In each iteration, first, a residual HR image is made by subtracting the component list identified in the previous iteration. Second, estimates are derived for the rms intensity in source-free regions using pixels more than 14 arcmin from the centre. No further components are added to the model, and the iterations are stopped if

- (i) the number of components in the model is six, or
- (ii) the peak in the residual HR image ≤ 4 times the rms in source free areas, or
- (iii) the image rms within 14 arcmin of the centre is within 10 per cent of the rms in source-free regions and no peak exceeds 5 times this rms.

New components are added to the component list in each iteration by locating the peak pixel in the residual HR image within 20 arcmin of the centre. An initial estimate of the flux density and position of this new component is derived by fitting a 7×7 -pixel HR-PSF beam patch to a 7×7 -pixel image patch around the position of the peak. Having updated the component list with this estimate for the parameters of the new component, the iteration ends by optimizing all the component parameters jointly by minimizing the variance in a residual HR image obtained by subtracting the components.

In Table 4 we have listed the components identified in the six

Table 4. Confusion models for the observed fields.

Field	Component flux density (μJy)	RA offset (arcmin)	Dec. offset (arcmin)
A2	183	-0.4	-0.3
	169	1.4	-1.2
	107	7.8	1.8
B1	253	1.1	-0.4
B2	321	0.4	0.9
	163	-0.6	-0.3
	99	-8.3	-3.9
	90	-9.1	-16.9
C1			
D1	455	-0.8	0.2
D2	94	-0.4	1.8

No sources were subtracted from field C1.

fields. It may be noted here that all components were constrained to be positive, and the estimation of component parameters did not use the LR images in any way. The residual LR and HR images obtained by subtracting these components are shown in Figs 3 and 4.

The rms of the pixel intensities in the residual LR and HR images, computed after weighting the pixels by the primary beam, are also listed in Table 3. It may be noted that the variance in these residual images are, in every case, in excess of the variance in the corresponding Stokes *V* images. The field B1 appears to have a significant negative feature close to the image centre. Visual comparisons between the residual LR and HR residual images do not show any correspondence in the positions of the peaks in the images.

The variance in the Stokes *V* images are a measure of the thermal noise in the images of the various fields. We have computed the weighted mean of the variances in the Stokes *I* images of the six fields, separately for the LR and HR images, using the Stokes *V* image variances as weights. Before subtracting the confusion models, the mean variance was $(51.7 \mu\text{Jy beam}^{-1})^2$ in the HR and $(117.1 \mu\text{Jy beam}^{-1})^2$ for the LR images; after confusion subtraction, the mean variances were $(25.0 \mu\text{Jy beam}^{-1})^2$ for the HR and $(52.0 \mu\text{Jy beam}^{-1})^2$ for the LR images. The weighted mean thermal noise (Stokes *V* image variance) is $(19.4 \mu\text{Jy beam}^{-1})^2$ for the HR and $(24.1 \mu\text{Jy beam}^{-1})^2$ for the LR images. The ‘excess’ variance is $(15.8 \mu\text{Jy beam}^{-1})^2$ for the HR and $(46.1 \mu\text{Jy beam}^{-1})^2$ for the LR images.

3.2 Residual confusion

Windhorst et al. (1993) have derived the radio source counts at μJy flux densities using deep images made at 8.44 GHz with the

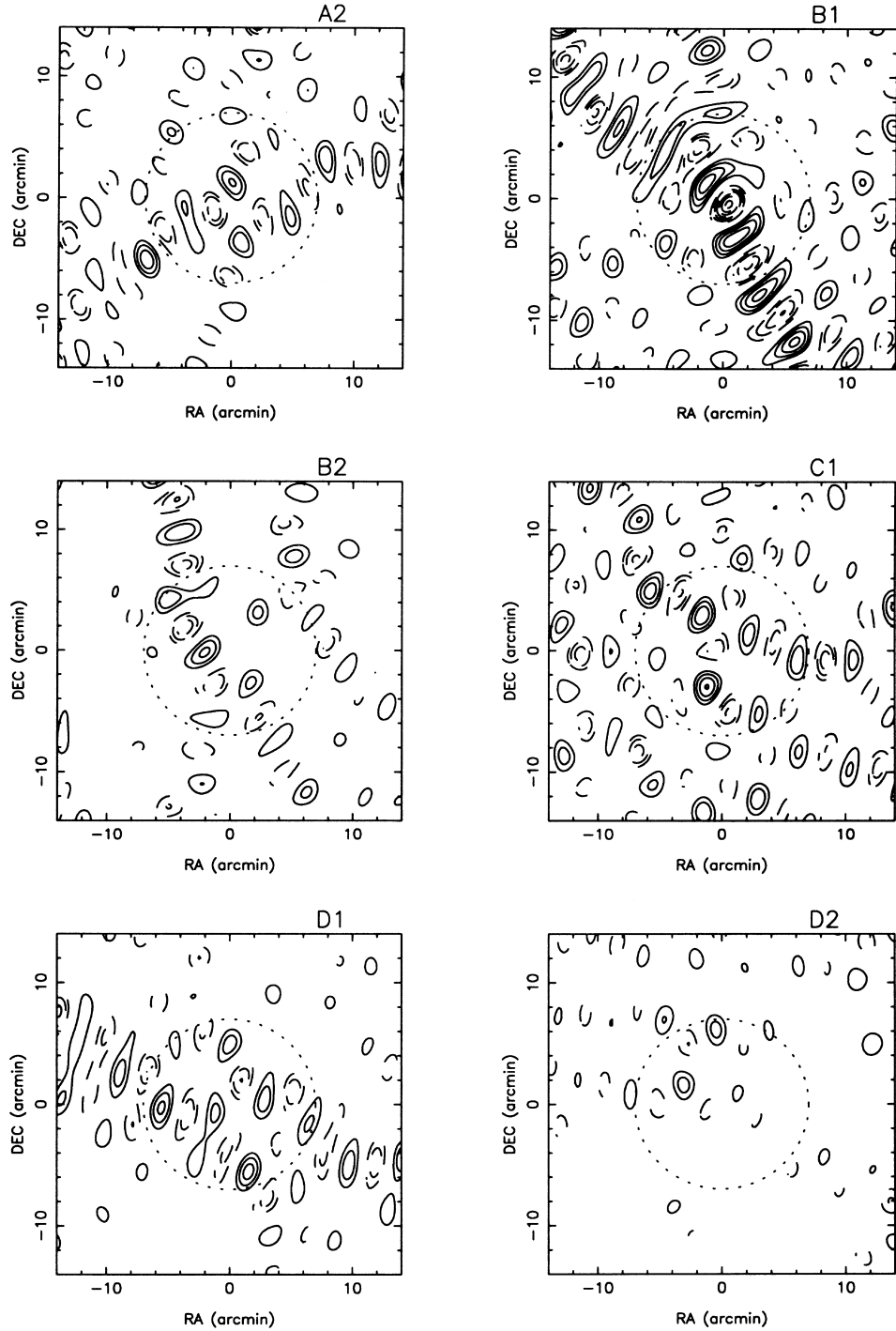


Figure 3. LR images of the six fields in Stokes I with the sources listed in Table 4 subtracted. Contours at $24.2 \mu\text{Jy beam}^{-1} \times (-8, -7, -6, -5, -4, -3, -2, 2, 3, 4, 5)$. Using equation (10), we may regard these images as representing contours of brightness temperature at $28.7 \mu\text{K} \times (-8, -7, -6, -5, -4, -3, -2, 2, 3, 4, 5)$.

VLA. Adopting a mean spectral index $\alpha = -0.5$ at these frequencies, the differential source counts are

$$\frac{dN}{dS} = (-5.05 \pm 0.80) \times 10^{-3} S_{40 \mu\text{Jy}}^{-2.3 \pm 0.2} \mu\text{Jy}^{-1} \text{arcmin}^{-2} \quad (2)$$

when scaled to 8.7 GHz. $S_{40 \mu\text{Jy}}$ denotes the flux density in units of $40 \mu\text{Jy}$, and the errors in the normalization and in the index are for a power-law fit that has the flux density S normalized to $40 \mu\text{Jy}$.

We have simulated skies with a Poisson random distribution of

faint sources, adopting the source counts given in equation (2) with the nominal values quoted for the normalization and index. Areas of the sky of about 2arcmin in diameter, roughly corresponding to the half-power areas of the synthesized beams of the LR images, would be expected to have one source on the average exceeding $70 \mu\text{Jy}$. In the simulations, sources in the flux density range 0.1 – $500 \mu\text{Jy}$ were included: because the differential source counts scale as $(dN/dS) \sim S^{-2.3}$, the variance contribution from sources in logarithmic intervals in flux density would scale

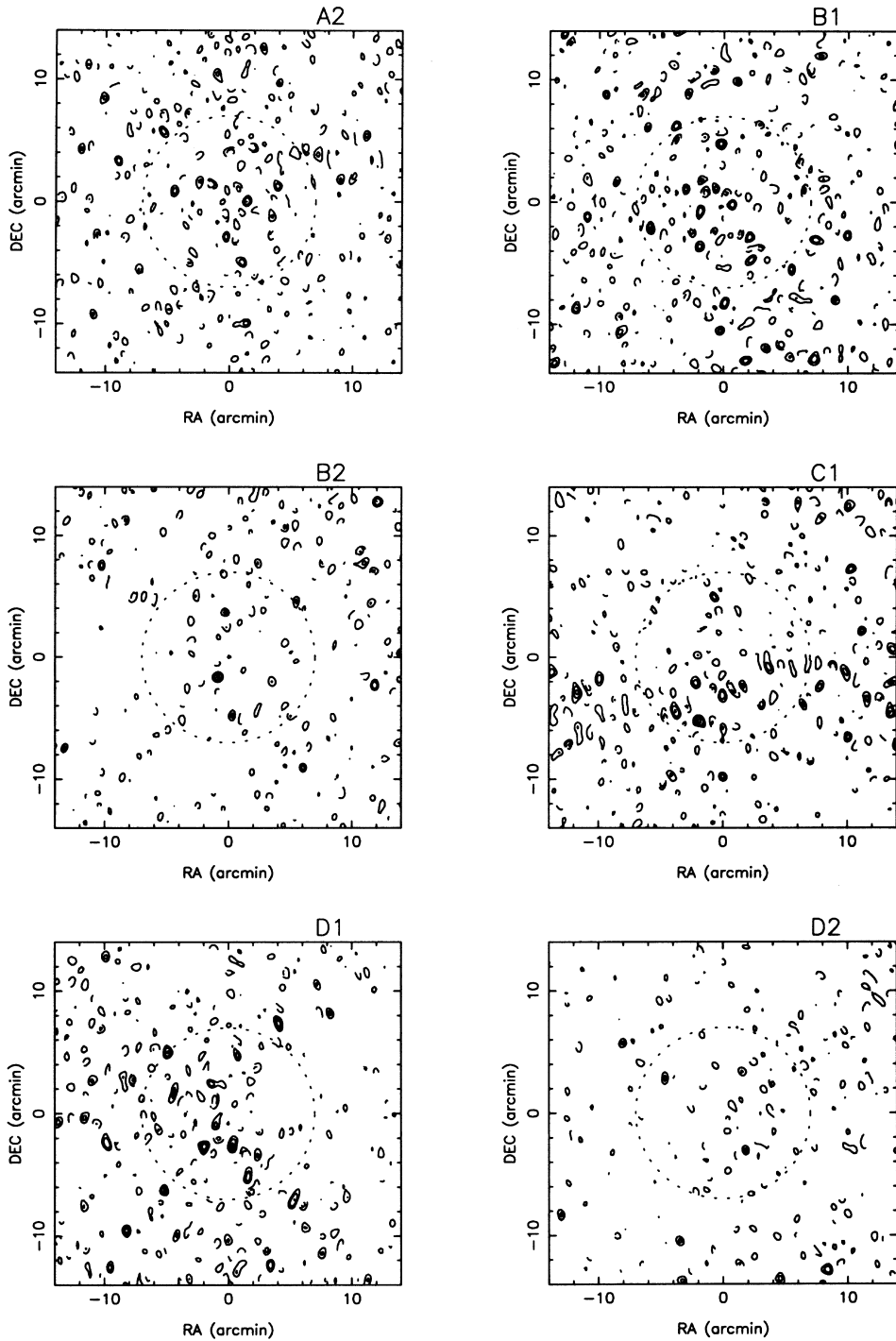


Figure 4. HR images of the six fields in Stokes I after subtracting the sources listed in Table 4. Contours at $19.5 \mu\text{Jy beam}^{-1} \times (-4, -3, -2, 2, 3, 4)$. From the telescope filter function corresponding to the HR beam, we derive the relation $\Delta S = 0.15 Q_{\text{flat}}$. Using this factor, the contours may be regarded as being at $131 \mu\text{K} \times (-4, -3, -2, 2, 3, 4)$.

as $\sigma^2 \sim S^{0.7}$, implying that weak sources below this range – which may be expected to be present in large numbers in every synthesized beam – would contribute little to the image variance. Our fields are selected to be devoid of strong sources exceeding $0.5 \mu\text{Jy}$.

For the simulations, weighted-mean synthesized beam patterns were computed by combining all the visibilities (of all the six fields) and computing LR and HR synthesized beams for the combined data base. In each simulation, the sources were

convolved by these beam patterns to produce separate LR and HR images. Thermal noise, whose autocorrelation was consistent with the square of the corresponding synthesized beam patterns, and with variance $(19.4 \mu\text{Jy beam}^{-1})^2$ for the HR and $(24.1 \mu\text{Jy beam}^{-1})^2$ for the LR images, were added to the simulated images.

The simulated images were processed by the same algorithm, described in Section 3.1, to subtract discrete source confusion. The residual LR images had a mean variance of $(58.8 \mu\text{Jy beam}^{-1})^2$, whereas the HR images had a mean variance of

($24.5 \mu\text{Jy beam}^{-1}$)². We have grouped the simulations in lots of six, to simulate our observations of six independent fields, and computed the mean residual variance in the groups of six fields. Their distribution implies that the observed rms pixel intensity, when computed as an average over six residual LR fields, may be expected to have a $\pm 1\sigma$ spread of $50.8\text{--}65.8 \mu\text{Jy beam}^{-1}$. The corresponding $\pm 1\sigma$ spread in the HR image rms values is $23.2\text{--}25.6 \mu\text{Jy beam}^{-1}$. The observed values of the rms pixel intensity as computed from the residual LR and HR images are 52.0 and $25.0 \mu\text{Jy beam}^{-1}$, and lie within the expected $\pm 1\sigma$ spreads.

The conclusion we make from the simulations is that the ‘excess’ variance we observe in the LR as well as HR images, after subtracting the derived confusion models, is consistent with the ‘excess’ expected from undetected weak sources. All of the ‘excess’ variance may be attributed to unsubtracted confusion.

4 FIELD B1

The residual image of field B1, in Fig. 3, shows a significant negative close to the field centre. A fit to the LR visibility data yields a value of $-202 \mu\text{Jy}$ and a position offset -17 arcsec in RA and -28 arcsec in Dec. from the field centre. The peak of the negative feature is 7.5 times the rms thermal noise. The corresponding residual HR image of field B1, shown in Fig. 4, shows no evidence for any negative at this sky position: the HR image value at the position of the negative (in the LR image) is $70 \mu\text{Jy beam}^{-1}$.

It may be noted here that the negative peak in the LR image of the residual B1 field (Fig. 3) does not appear to have the sidelobe pattern expected for an unresolved negative source: this means either that the negative source has structure on this scale or that the negative arises from a chance superposition of negative sidelobes of weak confusing sources in the field.

With the aim of examining the reality of this feature, we made a separate observation of the field with the ATCA antennae pointed towards position RA(J2000) = $01^{\text{h}}43^{\text{m}}37\text{.}36$, Dec.(J2000) = $-50^{\circ}58'27\text{''}33$. This field centre was offset 2.2 arcmin (-127 arcsec in RA and -32 arcsec in Dec.) from the previous pointing centre. We refer to this field centre as B1_OFFSET. The $253\text{-}\mu\text{Jy}$ source detected in the HR image of the B1 field is now 3.2 arcmin

from the field centre and may be expected to appear in the HR image of the B1_OFFSET field with a flux density of $120 \mu\text{Jy}$. Because the shift corresponds to about 40 per cent of the primary beam FWHM, we may expect a significant change in the image fluctuations that arise from the numerous weak sources in the sky. The position of the negative peak, which was seen in the residual B1 image, should now be 1.8 arcmin from the new field centre. Correcting for the attenuation due to the primary beam, we may expect the negative to appear with a value $-159 \mu\text{Jy beam}^{-1}$.

We display HR and LR images of the B1_OFFSET field in Fig. 5. No sources have been subtracted from these images. The rms thermal noise is $53 \mu\text{Jy beam}^{-1}$ in the LR image and $42 \mu\text{Jy beam}^{-1}$ in the HR image as estimated from the corresponding Stokes V images. At the position in the HR image, where we expect a $120 \mu\text{Jy}$ source, the pixel intensity is $73 \mu\text{Jy beam}^{-1}$. At the position of the possible decrement (indicated by the star symbol in Fig. 5), the pixel intensity is $-45 \mu\text{Jy beam}^{-1}$. The negative is not seen at the 2σ level.

We have examined the residual LR images created by our simulations to infer the decrements that may be expected from the negative sidelobes of residual unsubtracted positive confusing sources in the fields. We find that one in six fields may be expected to have a decrement exceeding $-250 \mu\text{Jy beam}^{-1}$. A decrement of the magnitude observed in Field B1, which is $-206 \mu\text{Jy beam}^{-1}$, may be expected in 35 per cent of the observed fields. The simulations indicate that the observed decrement in B1 may well be owing to residual confusion.

Because the B1_OFFSET image has not confirmed the decrement, and because the decrement in the B1 field does not have the sidelobe structure expected, we are led to question the reality of the decrement. We hypothesize that the decrement probably arises as a result of (i) weak confusion in the LR B1 image, and (ii) as a result of errors in the parameter estimates of the strong confusing source seen in the HR image of field B1: these errors may be due to confusion in the HR image.

5 HOLES IN THE MICROWAVE SKY?

In any sky image made at f_{GHz} GHz with a beam which has a half-maximum size of $\theta \text{ arcmin} \times \phi \text{ arcmin}$, the measured flux density

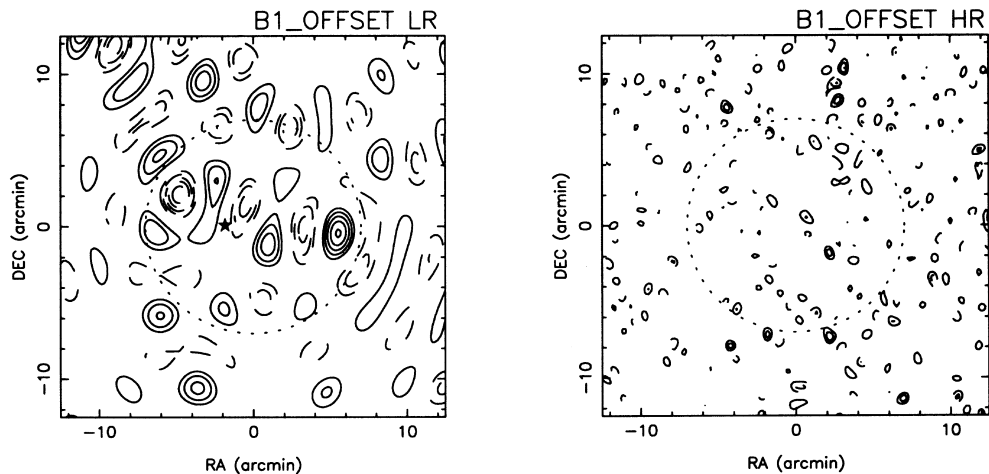


Figure 5. LR and HR images of the B1_OFFSET field. The field centre is shifted 2.2 arcmin from the centre of the B1 field. No sources have been subtracted. Contours at $40 \mu\text{Jy beam}^{-1} \times (-6, -5, -4, -3, -2, 2, 3, 4, 5, 6)$. The position of the possible negative decrement is indicated by the star symbol in the LR image. We may regard these images as representing contours of brightness temperature at $(-6, -5, -4, -3, -2, 2, 3, 4, 5, 6) \times 47 \mu\text{K}$ for the LR image and $270 \mu\text{K}$ for the HR image.

Table 5. Peak decrements observed in the residual LR images.

Field	(μ Jy beam $^{-1}$)	(μ K)
A2	-178	-254
B1	-206	-311
B2	-192	-275
C1	-93	-131
D1	-162	-232
D2	-108	-153

The average half-maximum beamsize in the LR images is 106 arcsec.

decrement (ΔS_{Jy}) at any image pixel may be converted to brightness temperature units using the relation

$$\Delta T = 4.6 \left(\frac{8.6}{f_{\text{GHz}}} \right)^2 \left(\frac{1}{\theta \times \phi} \right) \Delta S_{\text{Jy}}. \quad (3)$$

In Table 5 we have listed the peak decrement detected in each of the six fields observed. The values are listed for the residual LR images and are computed over the half-power areas of the primary beams (regions of 3-arcmin radius) and using images that have been corrected for the attenuation due to the primary beam. These values for the peak decrements may be considered limits on the magnitude of any decrements in the fields for comparisons with models predicting S-Z source counts in blank sky regions.

It may be noted here that the peak decrements listed in Table 5 for the fields A2, D1 and, in particular, B2 appear similar to the decrement listed for field B1. However, the peak decrements seen in the A2, D1 and B2 fields are all located almost 3 arcmin from the field centres and appear (in images prior to corrections for the attenuation due to the primary beam) at levels less than 4 times the thermal rms noise. On the other hand, the decrement in the B1 field is seen at a level 7.5 times the rms thermal noise and is located 0.5 arcmin from the field centre.

The sky area searched for decrements, in Table 5, is six fields of size 3 arcmin in radius, corresponding to a total of 0.05 deg 2 . The limit to the magnitude of decrements in this sky area is about 0.2 mJy at 8.7 GHz.

The S-Z decrement in the CMB brightness temperature has been detected along the lines of sight to several clusters of galaxies (see Birkinshaw 1998 for a recent review). For example, an interferometric image of the high-redshift cluster Cl 0016+16 ($z = 0.541$) with a beam of arcminute size showed a decrement corresponding to $-426 \mu\text{K}$; at a lower redshift, Abell 773 has been seen to show a $-312 \mu\text{K}$ dip (Carlstrom, Joy & Grego 1996). The S-Z decrements detected towards clusters of galaxies in targeted observations have yielded central decrements of several hundred μK . The decrement observed along lines of sight through the centre of a cluster depends on the integral of the thermal gas pressure along the path and is independent of the distance to the cluster; therefore it is unlikely that any rich cluster of galaxies lies in the surveyed region.

Several authors have estimated the CMB anisotropies caused by cosmological populations of clusters of galaxies (Bartlett & Silk 1994; Markevitch et al. 1994; Barbosa et al. 1996). Bartlett, Blanchard & Barbosa (1998) estimate the S-Z source counts at 0.75-mm wavelength, adopting the Press-Schechter formalism for the mass function and normalizing the matter density power spectrum to the present-day cluster abundances as measured by

the X-ray temperature distribution function. The limit from the ATCA observations translates to a limit of 30-mJy flux density at 0.75-mm wavelength. In an $\Omega_0 = 1$ universe, we may expect about 0.1 sources in the ATCA survey region; in an $\Omega_0 = 0.2$ universe, the expectation is about one source. The ATCA survey places constraints on models with $\Omega_0 < 0.2$.

Two separate interferometric images made of sky regions devoid of obvious clusters appear to have detected decrements. Jones et al. (1997) report a $\sim 410 \mu\text{Jy}$ integrated decrement in an RT image, containing a pair of quasars, made with a $110 \times 175 \text{ arcsec}^2$ beam at a frequency of 15 GHz. A second field showed no decrement. These correspond to one $\sim 20 \mu\text{Jy}$ S-Z source at 0.75 mm wavelength in 0.034 deg 2 sky area. Richards et al. (1997) report a $\sim 27 \mu\text{Jy}$ integrated flux density feature in their 30-arcsec resolution Very Large Array (VLA) images at 8.4 GHz. A separate VLA field observed previously showed no such decrement. The VLA results correspond to one 4-mJy source at 0.75 mm in a sky area of 0.018 deg 2 . These limits, as well as results from the SuZIE (Church et al. 1997) and OVRO RING experiments (Myers, Readhead & Lawrence 1993) are compared with the expected S-Z source counts by Bartlett et al. (1998).

The constraints imposed on the source counts by the ATCA survey are the same as those inferred from the other experiments. It may be noted, however, that (i) the ATCA survey region considerably exceeds the sky areas covered in the other interferometric imaging surveys, and (ii) the ATCA survey is truly a ‘blank field’ search as against the RT images which were made towards fields known to have quasars. We would also like to point out that the residual variance in the fields are dominated by, and consistent with, the expectations from residual unsubtracted confusion: constraining the S-Z source counts to be limited to the allowed residual variance, after accounting for the variance from weak unsubtracted confusion, will be expected to provide better limits on S-Z sources and hence on allowed cosmological models.

6 GAUSSIAN-FORM CMB ANISOTROPIES

Some CMB anisotropies may be modelled as being Gaussian random in their temperature distribution. As discussed earlier, these anisotropies are usually (and completely) described by the power spectrum which is the distribution of $l(l+1)C_l$ in l -space. The complex spectral amplitudes at different multipole orders are assumed to be random phase, and the fluctuations on different scales are assumed to be uncorrelated.

Assuming further that the anisotropy spectrum is flat implies that $l(l+1)C_l$ is a constant in l -space. The spectrum is then completely specified by its normalization, which may be parametrized as

$$l(l+1)C_l = \left(\frac{24\pi}{5} \right) (Q_{\text{flat}})^2. \quad (4)$$

The flat-spectrum CMB anisotropy results in a sky variance given by

$$(\Delta T)^2 = \sum_l \frac{6(2l+1)}{5l(l+1)} (Q_{\text{flat}})^2. \quad (5)$$

The normalization Q_{flat} is referred to as the quadrupole normalization because $(\Delta T)^2 = (Q_{\text{flat}})^2$ for $l = 2$, implying that Q_{flat} is the rms of the quadrupole anisotropy.

6.1 ATCA telescope filter function

In any CMB anisotropy experiment, the instrument characteristics, observing strategy and data analysis method together determine a ‘telescope filter function’ (TFF), which is an l -space filter F_l that defines the sensitivity of the observation to the CMB anisotropy power in different multipole orders. The ATCA LR images at 8.7 GHz have a beam of about 2 arcmin and this scale corresponds to multipole orders of several thousand. In the large- l limit, the LR image rms ΔS expected from a flat-spectrum CMB anisotropy spectrum may be approximately written in the form

$$(\Delta S)^2 = (Q_{\text{flat}})^2 \sum_l \frac{12}{5l} F_l, \quad (6)$$

where F_l has units $(\text{Jy beam}^{-1} \text{K}^{-1})^2$. As discussed in appendix A of Subrahmanyan et al. (1998), the TFFs vary across the synthesized image and may be computed at any image pixel position (θ_o, ϕ_o) from the ‘product beam’ $b(\theta, \phi)$, which is the product of the primary beam centred at the antenna pointing centre and the synthesized beam centred at (θ_o, ϕ_o) . The TFF is given by

$$F_l = \frac{1}{2\pi} \int_0^{2\pi} |\mathbb{F}(l, \xi)|^2 d\xi \left(\frac{2k}{\lambda^2} \right)^2, \quad (7)$$

where

$$\mathbb{F}(l, \xi) = \int \int b(\theta, \phi) e^{i(l\cos\xi + \phi l \sin\xi)} d\theta d\phi. \quad (8)$$

The sky variance was estimated as a weighted average of the variances in the six LR residual images; the weights used were inversely proportional to the thermal-noise variances. Therefore the synthesized beam used in the computation of the TFF was obtained by concatenating all the LR data and constructing a synthesized beam pattern by weighting the data based on the system temperatures recorded along with the individual visibility measurements. Because the rms in the individual images were computed by weighting the pixels using the primary-beam pattern, the TFFs computed at different image pixel positions were averaged using the squared primary-beam pattern as weights. The resulting ATCA TFF is shown in Fig. 6. The filter function F_l peaks at $l = 4900$ and has half-maximum values at $l = 3520$ and 6200 . Summing over the filter values yields

$$\sum_l \frac{12}{5l} F_l = 0.713 \left(\frac{\mu\text{Jy beam}^{-1}}{\mu\text{K}} \right)^2. \quad (9)$$

A flat-spectrum CMB anisotropy spectrum with normalization

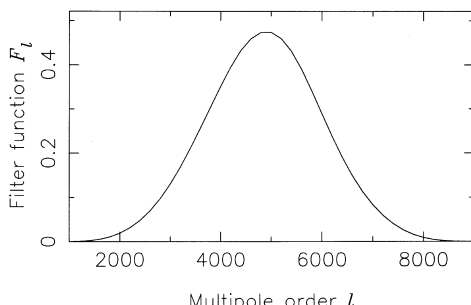


Figure 6. ATCA telescope filter function corresponding to the sky variance estimate that was derived as a weighted mean of the variances in the six LR residual images.

Q_{flat} would, consequently, be expected to result in an image rms

$$\Delta S = 0.844 Q_{\text{flat}}, \quad (10)$$

where Q_{flat} has units of μK , and ΔS is in $\mu\text{Jy beam}^{-1}$.

It may be noted here that the aperture illumination of the ATCA antenna – apart from the visibility-domain (u, v) -track of the 30.6-m baseline – determines the shape of the TFF profile. We have modelled the primary-beam pattern in the aperture domain, taking into account the central blockage of the Cassegrain optics and a radial aperture illumination profile. The parameters were determined from measurements of the beam pattern.

6.2 Polarized CMB anisotropies

The visibility data on the six fields have been used to construct LR images in Stokes Q and U in a search for polarized anisotropies on arcminute scales. The image rms were computed separately for the six fields after weighting the image intensities by the antenna primary-beam pattern, and these values are listed in Table 6. As discussed earlier, the expected image rms due to thermal noise may be derived from the corresponding Stokes V images, and these values are also listed in the table for comparison.

We have used the thermal-noise variances (variance in the corresponding Stokes V images) as weighting factors and computed the mean variance in the Stokes Q images to be $(22.2 \mu\text{Jy beam}^{-1})^2$ and that in the Stokes U images to be $(21.8 \mu\text{Jy beam}^{-1})^2$. The weighted-mean thermal noise is $24.1 \mu\text{Jy beam}^{-1}$. There does not appear to be any ‘excess’ variance in the polarized intensity images.

Examining the images without any correction for the primary-beam attenuation, the image intensities within the main lobes of the primary beams (within 7 arcmin of the image centres) are seen to be in the range $+86$ to $-81 \mu\text{Jy beam}^{-1}$. Simulations of LR images that contain exclusively a thermal-noise variance of $24.1 \mu\text{Jy beam}^{-1}$ reveals that the image intensities may be expected to span the range $\pm 82 \mu\text{Jy beam}^{-1}$ in any random sample containing 12 images. We conclude that the Stokes Q and U images of the six fields do not contain any features apart from those expected due to thermal noise.

Following the procedure described in Subrahmanyan et al. (1998), we have simulated sky images assuming that the sky is devoid of sources – this is probably a reasonable assumption for the Stokes Q and U images – and contains only flat-spectrum CMB variance. The polarized intensity LR images may be assumed to have contributions from thermal noise and any polarized CMB fluctuations: because the fluctuations owing to these two contributors would be uncorrelated, we have separately simulated images containing CMB fluctuations and thermal noise.

Table 6. Rms pixel intensities in Stokes Q , U and V images.

Field	Stokes Q	Stokes U	Stokes V
A2	25.2	28.6	23.9
B1	24.5	20.5	26.9
B2	25.4	20.6	23.0
C1	24.0	24.0	25.5
D1	28.5	15.7	23.0
D2	18.4	19.8	22.8

All rms noise values are in $\mu\text{Jy beam}^{-1}$. The rms in these Stokes Q and U images were computed from pixel intensities weighted by the primary beam.

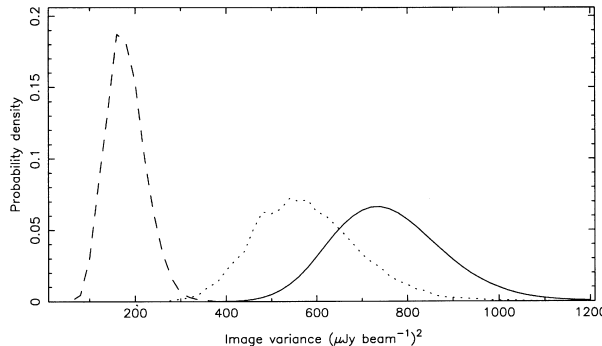


Figure 7. Likelihood functions – derived from simulations – that refer to the case of the Stokes Q and U images where there is no significant discrete source confusion. The dotted line represents the probability distribution of the thermal-noise contribution to the observed image variance. The dashed line is the distribution expected for the CMB variance contribution, assuming $Q_{\text{flat}} = 16 \mu\text{K}$. The continuous line is the convolution of these two curves, and represents the likelihood of obtaining any observed variance conditional on $Q_{\text{flat}} = 16 \mu\text{K}$.

Variance estimates are derived from the simulations – separately for the thermal noise and CMB contributions – in the same fashion as for the observations: the primary-beam weighted rms is derived for each simulated image, and the average variance is computed for sets of six images. In Fig. 7 we show the probability distributions for the variance contributions as inferred from the simulations; the CMB anisotropy has been assumed to have $Q_{\text{flat}} = 16 \mu\text{K}$, and the thermal noise in the LR images is assumed to have an rms of $24.1 \mu\text{Jy beam}^{-1}$. It may be noted here that these distribution functions do not follow a simple chi-square functional form, because the image variances have been estimated as a weighted sum of the squares of the pixel intensities. The mean variance in the simulated CMB-anisotropy images is $(13.6 \mu\text{Jy beam}^{-1})^2$, and this is consistent with that expected from the derived ATCA TFF (equation 10). The convolution of the two distribution functions – one for exclusively CMB anisotropy and the other corresponding to purely thermal noise – gives the distribution expected for the observed images, and this is also shown in Fig. 7. The result of the convolution represents the likelihood of observing any variance value assuming CMB anisotropy with $Q_{\text{flat}} = 16 \mu\text{K}$.

We use the likelihood-ratio test to derive upper limits on any polarized anisotropy in the CMB on arcminute scales. The null hypothesis \mathbb{H}_1 is that Q_{flat} is zero in the l -space window covered by the ATCA TFF, and that the observed LR images in polarized intensity have only thermal-noise variance. The likelihood function $\mathbb{P}(\sigma_{\text{obs}}^2 | 0)$ is the probability that the observed variance is σ_{obs}^2 , conditional on $Q_{\text{flat}} = 0$, and is given by the dotted line in Fig. 7. If we make the hypothesis \mathbb{H}_2 that the CMB anisotropy has a flat-band power Q_{flat} in addition to the expected thermal noise, the likelihood function $\mathbb{P}(\sigma_{\text{obs}}^2 | Q_{\text{flat}})$ gives the probability distribution of the observed variance. For the particular case of $Q_{\text{flat}} = 16 \mu\text{K}$, this likelihood function is given by the continuous curve in Fig. 7.

The decision variance is the observed variance σ_{obs}^2 . If we make the hypothesis \mathbb{H}_2 that the CMB anisotropy has a flat-band power exceeding Q_{flat} , the probability of rejecting this hypothesis when it is true is given by the integral of the likelihood function $\mathbb{P}(\sigma_{\text{obs}}^2 | Q_{\text{flat}})$ up to the decision variance σ_{obs}^2 . This integral is referred to as the size α of the test of hypothesis \mathbb{H}_2 ; $1 - \alpha$ is the confidence with which the observations with variance σ_{obs}^2 reject

the hypothesis. The probability of accepting the hypothesis \mathbb{H}_2 when the null hypothesis \mathbb{H}_1 is true defines the quantity $1 - \beta$, where β is referred to as the power of the test.

The observed variance in Stokes Q and U are less than the expected variance from thermal noise. If we adopt the values of the observed variances in Stokes Q and U as the decision variance to reject hypotheses, the tests will have powers $\beta < 0.5$. If choose to adopt the thermal-noise variance of $(24.1 \mu\text{Jy beam}^{-1})^2$ as the decision variance; this will yield tests with power $\beta = 0.5$. With this choice, we reject the hypothesis that Q_{flat} exceeds $16 \mu\text{K}$ with 95 per cent confidence. Adopting, instead, the observed Stokes Q variance of $(22.2 \mu\text{Jy beam}^{-1})^2$ as the decision variance, we conclude that $Q_{\text{flat}} < 11 \mu\text{K}$ with 95 per cent confidence; this test has a power $\beta = 0.23$. The corresponding limit based on the observed variance of $(21.8 \mu\text{Jy beam}^{-1})^2$ in Stokes U is $Q_{\text{flat}} < 10 \mu\text{K}$ with 95 per cent confidence and power $\beta = 0.17$.

6.3 Limits on flat-band total-intensity anisotropy

We derive limits on flat-band CMB anisotropies in total intensity from the LR images of the six surveyed fields. The residual images, shown in Fig. 3, are expected to have contributions from (i) the telescope thermal noise, (ii) fluctuations due to residual unsubtracted weak sources in the fields, and (iii) any CMB anisotropy. The weighted mean of the variances in the six residual LR Stokes I images was derived to be $(52.0 \mu\text{Jy beam}^{-1})^2$. As discussed earlier, the telescope thermal noise variance contribution is estimated to be $(24.1 \mu\text{Jy beam}^{-1})^2$ from the LR Stokes V images, and therefore there is a significant variance in the observed images apart from the thermal noise.

The simulations of discrete-source confusion, discussed in Section 3.2, indicated that if we adopt the nominal source counts given in equation (2), the residual images may be expected to have a variance of $(59 \pm 8 \mu\text{Jy beam}^{-1})^2$ owing to thermal noise and the unsubtracted confusion. This is consistent with the observed variance in the residual images and we conclude that there is no evidence in the LR images for any CMB anisotropy contribution.

It may also be noted that the HR residual images also have a significant variance in excess of the expected thermal noise – $(25.0 \mu\text{Jy beam}^{-1})^2$ as compared to the $(19.4 \mu\text{Jy beam}^{-1})^2$ thermal noise contribution – and this is also consistent with the simulations which predict a variance $(24.4 \pm 1.2 \mu\text{Jy beam}^{-1})^2$ for the combined contribution from thermal noise and residual confusion.

We assume that the sky fluctuations due to any CMB anisotropy is uncorrelated with the fluctuations due to thermal noise and residual confusion. The simulations described in Section 3.2, which provided random samples of images containing the expected contributions from thermal noise and residual confusion, were used to derive the expected distribution of image variance, conditional on $Q_{\text{flat}} = 0$. This distribution, $\mathbb{P}(\sigma_{\text{obs}}^2 | 0)$, is shown as the dotted line in Fig. 8, and represents the likelihood function for the null hypothesis \mathbb{H}_1 . The distribution function for the image variance contribution from a flat-band CMB anisotropy with $Q_{\text{flat}} = 28 \mu\text{K}$ is shown in Fig. 8 as a dashed line. The convolution of the two yields the continuous line in the figure and represents the likelihood function $\mathbb{P}(\sigma_{\text{obs}}^2 | Q_{\text{flat}})$ for the particular assumption that $Q_{\text{flat}} = 28 \mu\text{K}$. The observed variance in the Stokes I images, $(52.0 \mu\text{Jy beam}^{-1})^2$, rejects the hypothesis that Q_{flat} exceeds $28 \mu\text{K}$ with 95 per cent confidence.

The LR images, before any confusion subtraction, have an rms that exceeds the thermal noise rms by a factor of almost 5. After

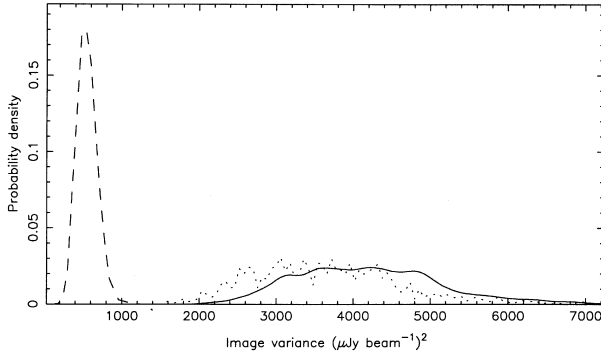


Figure 8. Likelihood functions – derived from simulations which include discrete-source confusion as well as thermal noise – that refer to the case of the Stokes I images. The dotted line represents the probability distribution of the combined contribution to the image variance from thermal noise + residual confusion. The dashed line is the distribution expected for the CMB variance contribution, assuming $Q_{\text{flat}} = 28 \mu\text{K}$. The continuous line is the convolution of these two curves, and represents the likelihood of obtaining any observed variance conditional on $Q_{\text{flat}} = 28 \mu\text{K}$.

subtracting the confusion models, the residual LR images are still confusion-limited, with an rms about 2 times higher than the thermal noise. Therefore the estimation of any CMB anisotropy contribution in the residual images is critically dependent on our knowledge of, and uncertainties associated with, the source counts at the 10- μJy level. Overestimations of the source-count normalization will result in spuriously low limits on any CMB anisotropy. However, we do not believe we have overestimated the expected discrete source counts because (i) the variance in the residual HR images exceeds the expected variance by 0.5σ , and (ii) the source counts derived by Partridge et al. (1997) in independent observations nominally exceeds the counts we have adopted here at the 10- μJy flux density level.

We have incorporated the uncertainties in the normalization and index of the differential source counts by simulating fields with Gaussian random choices of parameters for the source counts; we adopt 1-standard-deviation spreads for the parameters corresponding to the uncertainties quoted in equation (2). These simulations show, as may be expected, a 12 per cent increase in the standard deviation of image variances; however, the mean image variance is biased to a larger value: $(60.5 \mu\text{Jy beam}^{-1})^2$. Using this distribution as the likelihood function $\mathbb{P}(\sigma_{\text{obs}}^2 | 0)$ of the null hypothesis, and adopting the observed variance of $(52.0 \mu\text{Jy beam}^{-1})^2$ as the decision variance, we find that the observations rule out flat-band CMB anisotropy with $Q_{\text{flat}} > 25 \mu\text{K}$ with 95 per cent confidence.

6.4 Discussion

The 4-year COBE observations of CMB anisotropy (Bennett et al. 1996) correspond to a flat-band spectral power of $Q_{\text{flat}} = 18 \mu\text{K}$ in the multipole range $2 \leq l \leq 20$. Several experiments measuring anisotropies in l -space windows with centres located at multipoles up to a few hundred have reported detections corresponding to much greater spectral powers (see the website www.hep.upenn.edu/~max/cmb/experiments.html maintained by Max Tegmark for a compilation of experimental results). For example, the recent Python V results (Coble et al. 1999) report band powers rising from $Q_{\text{flat}} = 15$ to $63 \mu\text{K}$ over the multipole range $l = 50$ to 200 .

At multipoles exceeding $l \sim 10^3$, there are no reports to date of

the detection of Gaussian anisotropies in the CMB; observations have, however, detected isolated ‘holes’ in the CMB towards clusters of galaxies. As discussed earlier, the tentative detections of ‘holes’ in ‘blank fields’ are also presumably owing to the S–Z effect in distant clusters. The SuZIE experiment (Ganga et al. 1997) limit $Q_{\text{flat}} < 27 \mu\text{K}$ at the 2σ level in the multipole window $l = 1330$ – 3670 . RT observations of the Lynx 2 field (Jones 1997) limit $Q_{\text{flat}} < 12 \mu\text{K}$, or $\Delta T/T < 6.6 \times 10^{-6}$, in the window $4300 < l < 8300$ with 67 per cent confidence. The OVRO NCP experiment (Readhead et al. 1989) limit $\Delta T/T < 1.7 \times 10^{-5}$ at an angular scale of 2 arcmin. VLA images at 8.7 GHz limit $\Delta T/T < 2.0 \times 10^{-5}$ at an angular scale of 1 arcmin (Partridge et al. 1997). The VLA images also limit the sky anisotropy in linearly polarized intensity to $\Delta T/T < 1.0 \times 10^{-5}$ on the 1-arcmin scale.

The ATCA observations reported here cover six independent regions with a combined sky area of about 0.05 degrees². The images limit the CMB anisotropy in the multipole range $l = 3520$ – 6200 to $Q_{\text{flat}} < 25 \mu\text{K}$ in total intensity and $10 \mu\text{K}$ in linearly polarized fluctuations. These correspond to upper limits of $(\Delta T/T) < 6 \times 10^{-6}$ in linearly polarized intensity and $< 1.4 \times 10^{-5}$ in total intensity for fluctuations with an angular scale of 2 arcmin. The limits on polarized intensity fluctuations are the best to date; the limits on total intensity fluctuations are comparable to those set by other experiments on arcminute scales. These results are an improvement over the results published in Subrahmanyan et al. (1998) in that the inevitable confusion variance contribution to arcminute-scale sky fluctuations at 8.7 GHz has now been accounted for. The small-angle anisotropy experiments have consistently set limits that clearly establish the downturn in the CMB anisotropy spectrum between $l \sim 10^2$ and 10^3 .

7 CONCLUSIONS

We have made sensitive observations of six ‘blank’ fields with the aim of examining the arcminute-scale anisotropy in the CMB. After subtracting confusion models derived by higher resolution data, the residual images are consistent with the expected thermal noise and residual confusion from weak undetected sources. We do not believe we have detected any S–Z decrements in the blank fields. This data base is useful for deriving constraints (i) on the gas in cosmological distributions of clusters of galaxies, and (ii) on the CMB anisotropy power spectrum in total intensity and polarization at arcminute scales.

The variance in the images at 8.7 GHz is consistent with the expectations from thermal noise and the source counts at μJy flux density levels derived by Windhorst et al. (1993).

Assuming Gaussian-form CMB anisotropy with a ‘flat’ spectrum, we derive 95 per cent confidence upper limits of $Q_{\text{flat}} < 10$ – $11 \mu\text{K}$ in polarized intensity and $Q_{\text{flat}} < 25 \mu\text{K}$ in total intensity. These correspond to upper limits on $(\Delta T/T_{\text{CMB}})$ of 5.7 – 6.2×10^{-6} in polarized intensity and 1.4×10^{-5} in total intensity, where $T_{\text{CMB}} = 2.73 \text{ K}$ and $\Delta T = [l(l+1)C_l/2\pi]^{\frac{1}{2}}$. The ATCA filter function peaks at $l = 4700$ and has half-maximum values at $l = 3350$ and 6050 .

The ATCA observations are confusion-limited, and improvements in detection capability require observations at higher frequencies where the confusion is less. The ATCA is currently being upgraded to operate in the 16–25 GHz band, and a north spur is being added to the railtrack to allow two-dimensional close-packed array configurations. As discussed in Section 2, we expect the confusion noise to reduce as $\Delta S \sim \nu^{-2.2}$, and

observations at 18 GHz would have a confusion rms noise reduced by a factor of 5 as compared to the current observations at 8.7 GHz. The angular scale of the imaging would be reduced by a factor of 2 to about 1 arcmin. High-brightness-sensitive observations with an ultracompact ATCA at 18 GHz may improve limits on CMB anisotropy on arcminute scales. In particular, the upgrade would be useful in resolving the substructure in the X-ray gas of high-redshift clusters – detected in future blank-field S–Z surveys – by imaging their S–Z decrement.

The ATCA CMB anisotropy research website is located at www.atnf.csiro.au/research/cmbfr/cmbfr_atca.html.

ACKNOWLEDGMENTS

The Australia telescope is funded by the Commonwealth of Australia for operation as a National facility managed by CSIRO.

REFERENCES

Barbosa D., Bartlett J. G., Blanchard A., Oukbir J., 1996, *A&A*, 314, 13
 Bartlett J. G., Silk J., 1994, *ApJ*, 423, 12
 Bartlett J. G., Blanchard A., Barbosa D., 1998, *A&A*, 336, 425
 Bennett C. L. et al., 1996, *ApJ*, 464, L1
 Birkinshaw M., 1998, *Phys. Rep.*, 310, 97
 Bond J. R., Efstathiou G., 1984, *ApJ*, 285, L45
 Bond J. R., Jaffe A. H., 1998, *Phil. Trans. R. Soc. Lond. A*, ‘Discussion meeting on Large-scale Structure in the Universe’, Royal Society, London, 1998 March
 Carlstrom J. E., Joy M., Grego L., 1996, *ApJ*, 456, L75
 Church S. E. et al., 1997, *ApJ*, 484, 523
 Coble K. et al., 1999, *ApJ*, 519, L5
 Dodelson S., Jubas J. M., 1995, *ApJ*, 439, 503
 Ganga K., Ratra B., Church S. E., Ade P. A. R., Holzapfel W. L., Mauskopf P. D., Wilbanks T. M., Lange A. E., 1997, *ApJ*, 484, 523
 Gawiser E., Silk J., 1998, *Sci*, 280, 1405
 Gough R., 1994, Australia Telescope Technical Document AT/39.2/022

Hu W., White M., 1997, *New Astronomy*, 2, 323
 Hu W., Scott D., Silk J., 1994, *PRD*, 49, 648
 Hu W., Sugiyama N., Silk J., 1997, *Nat*, 386, 37
 Jones M. E., 1997, Proc. of the Particle Physics and the Early Universe Conference, Cambridge, 1997 April
 Jones M. E. et al., 1997, *ApJ*, 479, L1
 Large M. I., Mills B. Y., Little A. G., Crawford D. F., Sutton J. M., 1981, *MNRAS*, 194, 693
 Lawrence C. R., Scott D., White M., 1999, *PASP*, 111, 525
 Markevitch M., Blumenthal G. R., Forman W., Jones C., Sunyaev R. A., 1994, *ApJ*, 426, 1
 Metcalf R. B., Silk J., 1997, *ApJ*, 489, 1
 Molnar S. M., 1998, PhD thesis, Univ. Bristol
 Myers S. T., Readhead A. C. S., Lawrence C. R., 1993, *ApJ*, 405, 8
 Natarajan P., Sigurdsson S., 1999, *MNRAS*, 302, 288
 Partridge R. B., Richards E. A., Fomalont E. B., Kellermann K. I., Windhorst R. A., 1997, *ApJ*, 483, 38
 Readhead A. C. S., Lawrence C. R., Myers S. T., Sargent W. L. W., Hardebeck H. E., Moffet A. T., 1989, *ApJ*, 346, 566
 Richards E. A., Fomalont E. B., Kellermann K. I., Partridge R. B., Windhorst R. A., 1997, *AJ*, 113, 1475
 Seljak U., 1996, *ApJ*, 460, 549
 Subrahmanyan R., Ekers R. D., Sinclair M., Silk J., 1993, *MNRAS*, 263, 416
 Subrahmanyan R., Kesteven M. J., Ekers R. D., Sinclair M., Silk J., 1998, *MNRAS*, 298, 1189
 Subramanian K., Barrow J. D., 1998, *PRL*, 81, 3575
 The Australia Telescope, 1992, Special issue of *J. Electr. Electron. Eng. Aust.*, 12, June
 Windhorst R. A., Miley G. K., Owen F. N., Kron R. G., Koo D. C., 1985, *ApJ*, 289, 494
 Windhorst R. A., Fomalont E. B., Partridge R. B., Lowenthal J. D., 1993, *ApJ*, 405, 498
 Wright A. E., Griffith M. R., Burke B. F., Ekers R. D., 1994, *ApJS*, 91, 111
 Yamada M., Sugiyama N., Silk J., 1999, *ApJ*, 522, 66

This paper has been typeset from a *T_EX/L_AT_EX* file prepared by the author.